The Astrophysical Journal, 839:42 (11pp), 2017 April 10 https://doi.org/10.3847/1538-4357/aa68a0

Spectroscopic Evolution of Disintegrating Planetesimals: Minute to Month Variability in the Circumstellar Gas Associated with WD 1145+017

Seth Redfield[1], Jay Farihi[2], P. Wilson Cauley[1], Steven G. Parsons[3], Boris T. Gänsicke[4], and Girish M. Duvvuri[1]
[1] Astronomy Department and Van Vleck Observatory, Wesleyan University, Middletown, CT 06459, USA; sredfield@wesleyan.edu
[2] Department of Physics and Astronomy, University College London, London WC1E 6BT, UK
[3] Department of Physics and Astronomy, University of Sheffield, Sheffield, S3 7RH, UK
[4] Department of Physics, University of Warwick, Coventry CV4 7AL, UK
Received 2016 July 29; revised 2017 February 21; accepted 2017 February 27; published 2017 April 12

Abstract

With the recent discovery of transiting planetary material around WD 1145+017, a critical target has been identified that links the evolution of planetary systems with debris disks and their accretion onto the star. We present a series of observations, five epochs over a year, taken with Keck and the VLT, which for the first time show variability of circumstellar absorption in the gas disk surrounding WD 1145+017 on timescales of minutes to months. Circumstellar absorption is measured in more than 250 lines of 14 ions among 10 different elements associated with planetary composition, e.g., O, Mg, Ca, Ti, Cr, Mn, Fe, and Ni. Broad circumstellar gas absorption with a velocity spread of 225 km s^{-1} is detected, but over the course of a year blueshifted absorption disappears, while redshifted absorption systematically increases. A correlation of equivalent width and oscillator strength indicates that the gas is not highly optically thick (median $\tau \approx 2$). We discuss simple models of an eccentric disk coupled with magnetospheric accretion to explain the basic observed characteristics of these high-resolution and high signal-to-noise observations. Variability is detected on timescales of minutes in the two most recent observations, showing a loss of redshifted absorption for tens of minutes, coincident with major transit events and consistent with gas hidden behind opaque transiting material. This system currently presents a unique opportunity to learn how the gas causing the spectroscopic, circumstellar absorption is associated with the ongoing accretion evidenced by photospheric contamination, as well as the transiting planetary material detected in photometric observations.

Key words: circumstellar matter – line: profiles – minor planets, asteroids: general – stars: abundances – stars: individual (WD 1145+017) – white dwarfs

Supporting material: machine-readable table

1. Introduction

A rapid improvement in our understanding of the formation and evolution of exoplanetary systems is taking place using several distinct regions of the HR diagram. At the earliest stages, the Atacama Large Millimeter/submillimeter Array (ALMA) and similar observations of protoplanetary disks are leading to insights in early chemistry and physical structure (van der Marel et al. 2013; Öberg et al. 2015). In mature, solar-type, and low-mass stellar systems, *Kepler* transit observations and radial velocity studies are continuing to provide a bounty of exoplanetary systems in relatively close orbits, including numerous small and multi-planet systems (Vanderburg et al. 2016), but also true Jupiter analogs in colder orbits (Kipping et al. 2014). State-of-the-art adaptive optics systems are providing giant planet and substellar companion detections in relatively wide orbits at intermediate-mass stars (Carson et al. 2013; Macintosh et al. 2015), and for which a few iconic systems appear to share some broad characteristics of the solar system (Marois et al. 2008; Su et al. 2013). These detections cover a broad range of phase space that constrains planet frequency, size, and density as a function of stellar mass and metallicity, but there still remain critical, empirical gaps in our knowledge. For example, observational constraints on the interior structure of exoplanets are limited to model fits to the mean density (Madhusudhan et al. 2012) and extrapolating from the observations of the outermost atmospheric layers (Redfield et al. 2008; Miller-Ricci & Fortney 2010; Madhusudhan & Redfield 2015).

Fortunately, nature provides a means to indirectly measure the bulk chemistry of planetary precursors or fragments of major planets, via polluted white dwarfs. These "retired" systems also provide insight into small planets and their assembly around intermediate-mass stars, which is not yet possible with any current or planned technique. These advanced planetary systems are common. Their frequency is at least 30% (Zuckerman et al. 2010; Koester et al. 2014), providing a distinctive signature of exoplanetary systems (Farihi et al. 2013b; Rocchetto et al. 2015). While many exhibit the observational hallmarks of gaseous and dusty debris from tidally destroyed minor planets (Gänsicke et al. 2006; Farihi et al. 2009), due to the limited sensitivity of current infrared facilities to small planetesimal and disk masses (see Wyatt et al. 2014), numerous systems only reveal their planetary nature via atmospheric metals (Xu & Jura 2012; Bergfors et al. 2014). The atmospheric metal pollution itself enables the determination of the element to element abundances within the debris and disrupted parent body, where the most detailed measurements have yielded chemistry that is remarkably similar to the bulk Earth (Gänsicke et al. 2012; Jura & Young 2014), along with diversities comparable to but beyond the meteoritic classes of the solar system (Xu et al. 2013), and with some outstanding objects that are rocky yet H_2O-rich (Farihi et al. 2013a; Raddi et al. 2015).

Recent space and ground-based light curves of WD 1145+017 provide striking confirmation of the now-standard model, where atmospheric metals in white dwarfs originate from planetesimals disrupted near their stellar Roche limits. In the first campaign of the *Kepler* K2 operations, WD 1145+017 was identified and proposed by three groups to be observed (GO1071 PI: Redfield; GO1048 PI: Burleigh; GO1007 PI: Kilic), and these data revealed transits consistent with multiple, disintegrating asteroids around a star with a metal-polluted atmosphere. The observations exhibit a complex transiting signature of multiple bodies orbiting on periods of 4.5–4.9 hr (Vanderburg et al. 2015). This is the first white dwarf to be found to exhibit a transit signature. Extensive ground-based campaigns have been performed (e.g., Gänsicke et al. 2016; Rappaport et al. 2016; Croll et al. 2017). These photometric observations show a much higher incidence of transit activity than seen in the original K2 data. A wide diversity of transit shapes are also detected, indicating substantial evolution of the system in only a matter of months. While it is important to note that no object with a planetary mass or size has been detected orbiting a white dwarf, given the evidence of circumstellar gas and dust, together with transits of disintegrating dwarf planets, we hereafter refer to WD 1145+017 as a white dwarf planetary system. Indeed, we will refer to white dwarfs with detected debris disks as white dwarf planetary systems because, like WD 1145+017, the source of this debris is likely planetary in origin.

Xu et al. (2016) published high-resolution spectra of WD 1145+017 obtained by Keck. These observations show strong photospheric lines indicative of recent accretion onto the star, as well as distinct absorption profiles caused by circumstellar gas. The star exhibits a He-rich atmospheric spectrum punctuated by myriad, strong lines of heavy elements. Given the rapid settling time for heavy elements ($<10^6$ years, compared with $>10^8$ years cooling age), the circumstellar material has been recently accreted onto the stellar surface. Low-resolution ($\Delta\lambda \approx 1000$ Å) spectroscopic observations show transit events akin to photometric observations, with no significant variation by wavelength (Alonso et al. 2016).

The discovery of transiting events associated with WD 1145+017 comes right on the heels of several white dwarf planetary systems exhibiting variability, and implying dynamical evolution on human timescales. The first variations of any kind were seen in the gaseous emission lines associated with the disk orbiting Ton 345 (Gänsicke et al. 2008). The gas component in the disk at SDSS J122859.93+104032.9 has persisted for at least 12 years and may vary periodically (Manser et al. 2016), while similar emission from SDSS J161717.04+162022.4 has monotonically decreased, then disappeared over several years (Wilson et al. 2014). Photospheric line variability in calcium was identified by von Hippel & Thompson (2007) for G29-38, though follow-up analysis disputed these results (Debes & López-Morales 2008). Only within the past two years has variability also been witnessed via thermal emission in the infrared. A rapid drop in infrared emission has been seen in at least one system, SDSS J095904.69–020047.6, and it remains unclear how this might have occurred (Xu & Jura 2014). It has been suggested for some time that high-rate bursts of disk accretion take place onto polluted white dwarfs (Farihi et al. 2012; Metzger et al. 2012), and the necessary, highly dynamical formation of the compact disks (Veras et al. 2015) make such events likely, but as yet no variability associated with changes in accretion rate or metal abundance has been confirmed.

This paper explores the variability and richness of high-resolution spectra (five epochs over the course of a year) of WD 1145+017, and emphasize the unique opportunity to measure the physical conditions (e.g., abundances, dynamics, etc.) in the circumstellar disk. This so-far unique star provides an unprecedented window to observe planetesimal disintegration, catastrophic fragmentation, and disk evolution in real time.

2. Observations and Data Reduction

2.1. Keck/HIRES

Observations of WD 1145+017 were taken on 2015 November 14 using HIRES on Keck I (Vogt et al. 1994) as part of program 15B/N116Hb (PI: Redfield), to monitor polluted white dwarfs. The approximate resolving power of the observations is $R \equiv \lambda/\Delta\lambda \approx 34{,}000$, or $8.8\,\mathrm{km\,s^{-1}}$. The C5 decker was employed, which has a slit size of $7\farcs0 \times 1\farcs1$. Two 20 minute exposures were taken at the end of the night at high airmass. The signal-to-noise (S/N) per pixel of the extracted spectra is approximately 10 across much of the observed spectrum, which ranges from 3100–5890 Å.

The data were reduced using the HIRES Redux package written by Jason X. Prochaska.[5] Standard reduction steps were taken, including bias subtraction, flat fielding, and the removal of cosmic rays and hot pixels. The spectra were extracted using a $6\farcs6$ boxcar. All images were examined manually for order overlap in the blue chip. HIRES Redux also performs 2D wavelength solutions using ThAr lamp exposures taken at the beginning of each night. The residuals for the wavelength fits are ≈0.05 pixels, or ≈0.02 Å, in all orders. When applied to an individual observation, all wavelength solutions are corrected for Earth's heliocentric velocity.

We also make use of the Keck/HIRES spectra from program 15A/UCLA (PI: Jura), which were presented and made available by Xu et al. (2016). These are the earliest high-resolution spectra available on this target, taken before the announcement of the K2 detection by Vanderburg et al. (2015).

2.2. VLT/X-shooter

Observations of WD 1145+017 were performed with X-shooter (Vernet et al. 2011) on 2016 February 14, March 29, and April 8, under Director's Discretionary Time Program 296.C-5014 (PI: Farihi). For the February run, the science target was placed on the slit and observed in nodding mode in all three instrument arms quasi-continuously for 5.1 hr, while the star was above airmass 2.0. In the UVB, VIS, and NIR arms, respectively, the exposure times were 300, 366, and 2×188 s. Spectra were taken at four (ABBA) positions along the slit, separated by $5''$, before resetting the rotator to the parallactic angle. In total, there were 10 consecutive repetitions of this overall pattern, resulting in 40 separate exposures. Acquisition and guiding were carried out in an attempt to minimize slit losses due to the current lack of the atmospheric dispersion corrector on X-shooter. In order to increase S/N, the March and April runs were executed in stare mode for 2.9 and 5.0 hr, respectively. The exposure times were 280, 314, and 240 s in UVB, VIS, and NIR arms respectively. All observations were through slits of $0\farcs8$, $0\farcs9$, and $0\farcs9$ for UVB, VIS, and NIR, respectively, resulting in nominal resolving powers of

[5] http://www.ucolick.org/~xavier/HIRedux/

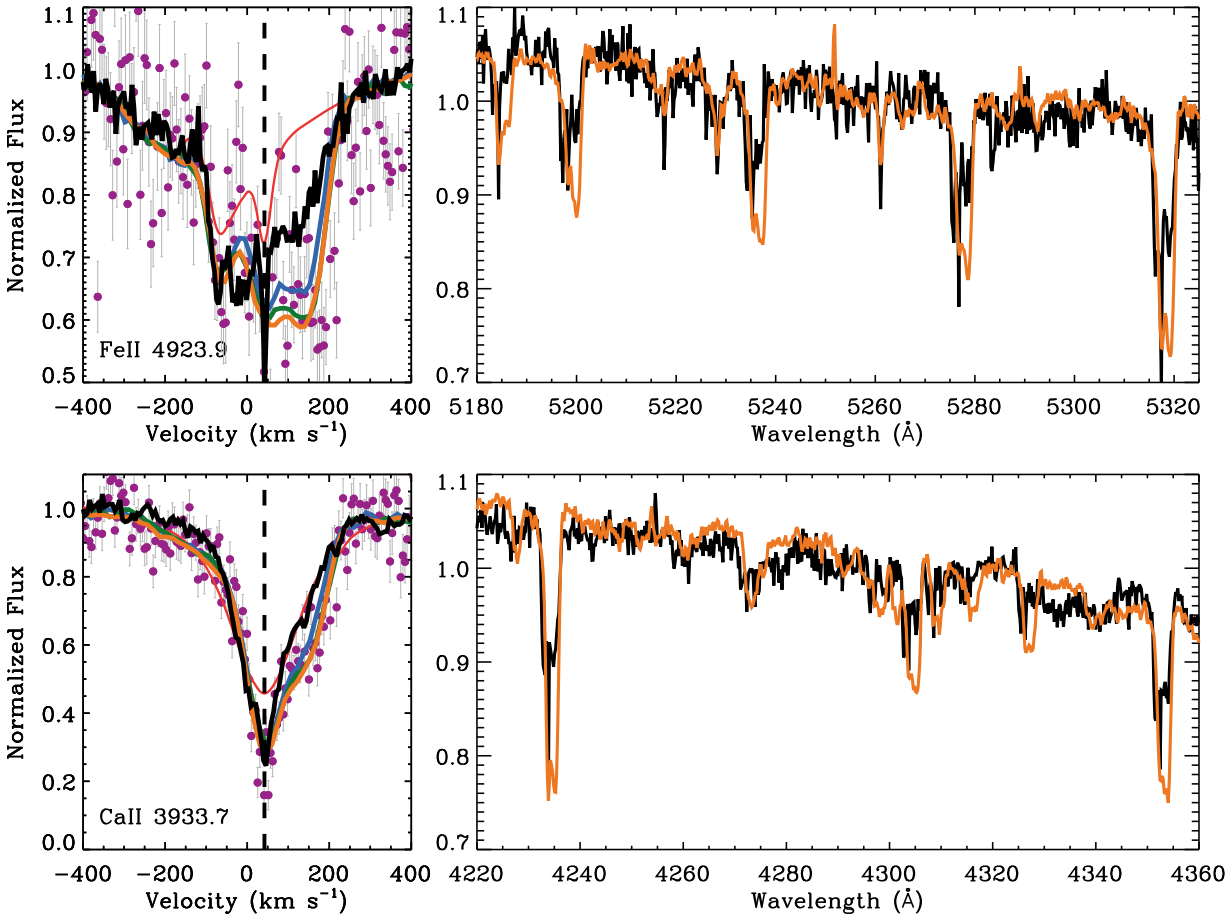

Figure 1. (Left) Individual profiles comparing spectra obtained for five epochs (Keck/HIRES 2015 April (black) presented in Xu et al. (2016) and 2015 November (purple) with 1σ error bars, and VLT/X-shooter 2016 February (blue), 2016 March (green), and 2016 April (orange). A photospheric model is shown in red. Clear circumstellar absorption is detected with (1) substantial variability on the red side of the feature, and (2) a diminishing of blueshifted features observed in the earliest data. (Right) Circumstellar features are ubiquitous in the spectrum. A broader wavelength region is displayed with only the the two most distant observations in time, VLT/X-shooter 2016 April in orange and Xu et al. (2016) Keck/HIRES spectrum in black.

$R \approx 6200$, 7450, and 5300. The optical chips were read out binned by 2 pixels in the spectral direction and in low-gain and high-speed mode to minimize dead time.

The X-shooter data were reduced using the latest release of the X-shooter Common Pipeline Library (CPL) recipes (version 2.6.8) within ESORex, the ESO recipe Execution tool, version 3.12. The standard recipes were used to extract and wavelength calibrate the data, the instrumental response was removed using twilight observations of the standard star EG 274. We found at optical wavelengths the additional flexibility of optimally reducing each spectrum individually lead to better results than the standard combination of ABBA nod sets. This is mainly due to the non-negligible curve of the spectrum introduced by differential atmospheric dispersion since the slit was not perfectly aligned at the parallactic angle despite our attempts to minimize this effect. This also led to relatively large slit losses at the shortest wavelengths, i.e., <3200 Å.

The optical spectral extractions were performed in two ways, with the pipeline assuming the data were taken in either nodding mode or staring mode (regardless of how the data were actually taken). Those extracted as if in staring mode were found to be clearly superior to those extracted as if in nodding mode, and thus only the former extractions were used in the analysis. Exposures taken with the NIR arm were found to have insufficient signal for useful results; the 40 frames taken during the February nodded observations resulted in an overall S/N < 5 in the H band.

3. Spectroscopic Features

We detect photospheric and circumstellar lines in multiple transitions and ions of the major elements involved in terrestrial planet formation: primarily Mg, Al, Si, Ca, Fe, and secondary trace elements such as Ti, Cr, and Ni. Figure 1 gives several examples of the circumstellar absorption profiles. Two lines (Fe II at 4923.9 Å and Ca II at 3933.6 Å) are shown in detail on the left. Larger segments of the spectrum are also shown comparing the first (2015 April; Xu et al. 2016) and last (2016 April) epochs, showing many examples of circumstellar absorption, mainly due to Fe II.

3.1. Photospheric

The photospheric metal abundances are measured by fitting white dwarf atmospheric models to the data with fixed $T_{\rm eff} = 15{,}900$ K and $\log g = 8.0$, as estimated in Vanderburg et al. (2015). The model and spectral fitting procedure are detailed in Koester (2010). Sharp photospheric lines are detected at a velocity of 42 km s^{-1}, with 30 km s^{-1} associated with the gravitational redshift given the assumed bulk properties of this white dwarf ($M_\star \approx 0.6\,M_\odot$ and $R_\star \approx 1.4\,R_\oplus$), and therefore 12 km s^{-1} associated with the radial velocity of the star. Note

Table 1
Detected Circumstellar Absorption Features and Fit Parameters

Ion	λ	E_{low}	E_{up}	log *gf*	EW	EW	EW	EW	EW	Comments[a]
					Keck/HIRES		VLT/X-shooter			
					2015 Apr	2015 Nov	2016 Feb	2016 Mar	2016 Apr	
	(Å)	(eV)	(eV)		(Å)	(Å)	(Å)	(Å)	(Å)	
Fe II	3227.742	1.67	5.51	−1.130	$0.328\pm^{0.031}_{0.030}$	$0.325\pm^{0.035}_{0.035}$	$0.596\pm^{0.047}_{0.043}$	$0.698\pm^{0.026}_{0.032}$	$0.768\pm^{0.017}_{0.035}$	i
Ni II	3576.764	3.07	6.54	−1.628	$0.181\pm^{0.015}_{0.014}$	$0.197\pm^{0.026}_{0.021}$	$0.501\pm^{0.021}_{0.018}$	$0.545\pm^{0.021}_{0.017}$	$0.549\pm^{0.010}_{0.013}$	i
Fe I	3647.842	0.91	4.31	−0.194	$0.026\pm^{0.004}_{0.004}$	$0.571\pm^{0.033}_{0.034}$	$0.083\pm^{0.017}_{0.016}$	$0.098\pm^{0.012}_{0.011}$	$0.140\pm^{0.015}_{0.007}$	i
Ca II	3933.663	0.00	3.15	0.134	$0.417\pm^{0.015}_{0.015}$	$0.395\pm^{0.023}_{0.023}$	$0.477\pm^{0.015}_{0.013}$	$0.462\pm^{0.010}_{0.008}$	$0.542\pm^{0.006}_{0.006}$	i
Ca II	3968.469	0.00	3.12	−0.166	$0.395\pm^{0.024}_{0.023}$	$0.366\pm^{0.018}_{0.017}$	$0.393\pm^{0.046}_{0.011}$	$0.520\pm^{0.006}_{0.006}$	$0.614\pm^{0.005}_{0.005}$	i
Fe I	4045.813	1.48	4.55	0.280	⋯	⋯	$0.107\pm^{0.010}_{0.009}$	$0.151\pm^{0.011}_{0.013}$	$0.187\pm^{0.006}_{0.006}$	i
Fe II	4173.461	2.58	5.55	−2.180	$0.101\pm^{0.013}_{0.012}$	$0.115\pm^{0.013}_{0.013}$	$0.165\pm^{0.008}_{0.007}$	$0.169\pm^{0.009}_{0.007}$	$0.199\pm^{0.021}_{0.005}$	i
Fe II	4178.862	2.58	5.55	−2.480	$0.111\pm^{0.012}_{0.011}$	$0.161\pm^{0.012}_{0.012}$	$0.236\pm^{0.011}_{0.009}$	$0.269\pm^{0.025}_{0.009}$	$0.265\pm^{0.005}_{0.008}$	i
Fe II	4233.172	2.58	5.51	−2.000	$0.272\pm^{0.009}_{0.007}$	$0.330\pm^{0.014}_{0.013}$	$0.584\pm^{0.026}_{0.041}$	$0.662\pm^{0.016}_{0.007}$	$0.721\pm^{0.004}_{0.005}$	i
Fe I	4325.762	1.61	4.47	−0.010	$0.021\pm^{0.005}_{0.005}$	$0.057\pm^{0.014}_{0.013}$	$0.117\pm^{0.010}_{0.012}$	$0.152\pm^{0.009}_{0.008}$	$0.183\pm^{0.006}_{0.005}$	i
Fe II	4351.769	2.70	5.55	−2.100	$0.213\pm^{0.008}_{0.008}$	$0.221\pm^{0.014}_{0.013}$	$0.416\pm^{0.009}_{0.010}$	$0.511\pm^{0.006}_{0.007}$	$0.546\pm^{0.004}_{0.004}$	i
Fe I	4404.750	1.56	4.37	−0.142	$0.029\pm^{0.009}_{0.008}$	$0.022\pm^{0.008}_{0.007}$	$0.056\pm^{0.008}_{0.007}$	$0.084\pm^{0.007}_{0.006}$	$0.104\pm^{0.004}_{0.005}$	i
Fe II	4508.288	2.86	5.60	−2.210	$0.128\pm^{0.012}_{0.011}$	$0.203\pm^{0.018}_{0.017}$	$0.267\pm^{0.018}_{0.012}$	$0.325\pm^{0.010}_{0.019}$	$0.338\pm^{0.005}_{0.004}$	i
Ti II	4533.969	1.24	3.97	−0.770	$0.454\pm^{0.784}_{0.441}$	$0.612\pm^{1.109}_{0.586}$	$0.041\pm^{0.010}_{0.008}$	$0.087\pm^{0.009}_{0.009}$	$0.097\pm^{0.006}_{0.006}$	i
Fe II	4549.474	2.83	5.55	−1.750	$0.251\pm^{0.017}_{0.016}$	$0.304\pm^{0.016}_{0.016}$	$0.403\pm^{0.023}_{0.017}$	$0.512\pm^{0.012}_{0.012}$	$0.574\pm^{0.009}_{0.016}$	i
Fe II	4583.837	2.81	5.51	−2.020	$0.289\pm^{0.008}_{0.008}$	$0.409\pm^{0.018}_{0.017}$	$0.610\pm^{0.021}_{0.013}$	$0.688\pm^{0.007}_{0.007}$	$0.745\pm^{0.004}_{0.004}$	i
Fe II	4629.339	2.81	5.48	−2.370	$0.119\pm^{0.008}_{0.008}$	$0.174\pm^{0.015}_{0.015}$	$0.267\pm^{0.020}_{0.014}$	$0.290\pm^{0.028}_{0.010}$	$0.324\pm^{0.004}_{0.004}$	i
Cr II	4824.127	3.87	6.44	−1.220	$0.025\pm^{1.047}_{0.013}$	$0.030\pm^{0.010}_{0.011}$	$0.049\pm^{0.015}_{0.013}$	$0.070\pm^{0.011}_{0.009}$	$0.091\pm^{0.013}_{0.010}$	i
Fe II	4923.927	2.89	5.41	−1.320	$0.459\pm^{0.027}_{0.024}$	$0.688\pm^{0.033}_{0.031}$	$1.182\pm^{0.027}_{0.025}$	$1.271\pm^{0.015}_{0.012}$	$1.402\pm^{0.008}_{0.031}$	i
Mg I	5183.604	2.72	5.11	−0.180	$0.070\pm^{0.008}_{0.008}$	$0.159\pm^{0.035}_{0.035}$	$0.147\pm^{0.012}_{0.012}$	$0.179\pm^{0.012}_{0.013}$	$0.188\pm^{0.007}_{0.007}$	i
Fe II	5234.625	3.22	5.59	−2.050	$0.173\pm^{0.011}_{0.010}$	$0.241\pm^{0.026}_{0.025}$	$0.397\pm^{0.011}_{0.013}$	$0.492\pm^{0.009}_{0.009}$	$0.512\pm^{0.004}_{0.005}$	i
Fe II	5276.002	3.20	5.55	−1.940	$0.239\pm^{0.012}_{0.013}$	$0.342\pm^{0.044}_{0.044}$	$0.472\pm^{0.012}_{0.011}$	$0.533\pm^{0.033}_{0.011}$	$0.583\pm^{0.012}_{0.016}$	i
Fe II	5316.615	3.15	5.48	−1.850	$0.313\pm^{0.012}_{0.011}$	$0.522\pm^{0.033}_{0.030}$	$0.654\pm^{0.022}_{0.018}$	$0.750\pm^{0.025}_{0.013}$	$0.882\pm^{0.005}_{0.005}$	i
Fe II	5362.869	3.20	5.51	−2.739	$0.143\pm^{0.011}_{0.010}$	$0.100\pm^{0.021}_{0.019}$	$0.246\pm^{0.016}_{0.014}$	$0.304\pm^{0.012}_{0.011}$	$0.308\pm^{0.010}_{0.007}$	i
Na I	5889.951	0.00	2.10	0.117	⋯	⋯	$0.297\pm^{0.028}_{0.039}$	$0.347\pm^{0.022}_{0.020}$	$0.408\pm^{0.016}_{0.026}$	i
Na I	5895.924	0.00	2.10	−0.184	⋯	⋯	$0.625\pm^{0.051}_{0.055}$	$0.692\pm^{0.043}_{0.039}$	$0.977\pm^{0.024}_{0.020}$	b
Fe II	6247.557	3.89	5.88	−2.329	⋯	⋯	$0.158\pm^{0.014}_{0.014}$	$0.244\pm^{0.017}_{0.015}$	$0.302\pm^{0.011}_{0.010}$	i
Fe II	6456.383	3.90	5.82	−2.075	⋯	⋯	$0.350\pm^{0.019}_{0.017}$	$0.374\pm^{0.024}_{0.023}$	$0.491\pm^{0.018}_{0.027}$	i
O I	7775.388	9.15	10.74	−0.046	⋯	⋯	$0.351\pm^{0.024}_{0.021}$	$0.443\pm^{0.024}_{0.022}$	$0.475\pm^{0.014}_{0.014}$	i
Ca II	8498.023	1.69	3.15	−1.312	⋯	⋯	$0.366\pm^{0.036}_{0.040}$	$0.453\pm^{0.024}_{0.025}$	$0.553\pm^{0.014}_{0.014}$	i
Ca II	8542.091	1.70	3.15	−0.362	⋯	⋯	$0.650\pm^{0.024}_{0.029}$	$0.732\pm^{0.029}_{0.024}$	$0.801\pm^{0.017}_{0.044}$	i
Ca II	8662.141	1.69	3.12	−0.623	⋯	⋯	$0.533\pm^{0.025}_{0.024}$	$0.763\pm^{0.035}_{0.044}$	$0.766\pm^{0.017}_{0.016}$	i

Note.
[a] (i) isolated feature; (b) blended feature.

(This table is available in its entirety in machine-readable form.)

that modest changes in the mass or radius of the star, of the order of 10%–20%, result in significant changes in the gravitational redshift, and therefore also in the estimated radial velocity of the system. The gravitational redshift could plausibly be anywhere between 25 and 45 km s^{-1} given reasonable white dwarf mass values (0.55–0.75 $M_{\odot}$). However, this does not prevent accurate modeling of the spectra.

The photospheric abundances in the new observations are consistent with the measurements by Xu et al. (2016) to within <0.2 dex for Mg, Al, Si, Ca, Fe, and the upper limit for C. For Ti, Cr, and Ni there are many lines, but all seem to be affected by circumstellar absorption, so a definitive abundance measurement is difficult. The only significant, though notable, discrepancy with the photospheric abundances presented in Xu et al. (2016) is that our O abundance is 0.2 dex lower.

Based on the published atmospheric metal abundances with modest updates from the modeling presented here, the composition of the debris accreted onto WD 1145+017 can be inferred. Using updated white dwarf diffusion models[6] (Koester 2009), both the early phase ($t < t_{diff}$) and steady state ($t \gtrsim 5t_{diff}$) abundances of the material can be calculated for O, Mg, Al, Si, Ca, and Fe.

Interestingly, the material polluting the atmosphere of WD 1145+017 is broadly chondritic in O, Mg, Al, and Si, but shows significant enhancements in both Ca and Fe. This is a curious mix of material that, at least superficially, appears to be a mixture of crust-like and core-like matter. Relative to the expected oxide minerals of Mg, Al, Ca, and Fe (Klein et al. 2010), the abundance pattern also supports a modest excess of oxygen in the accreted matter. This excess amounts to 45% or 60% by mass for the steady state or early accretion phases, respectively (Farihi et al. 2013b), with the more conservative number yielding a water mass fraction of 20%. If

[6] http://www1.astrophysik.uni-kiel.de/~koester/astrophysics/astrophysics.html

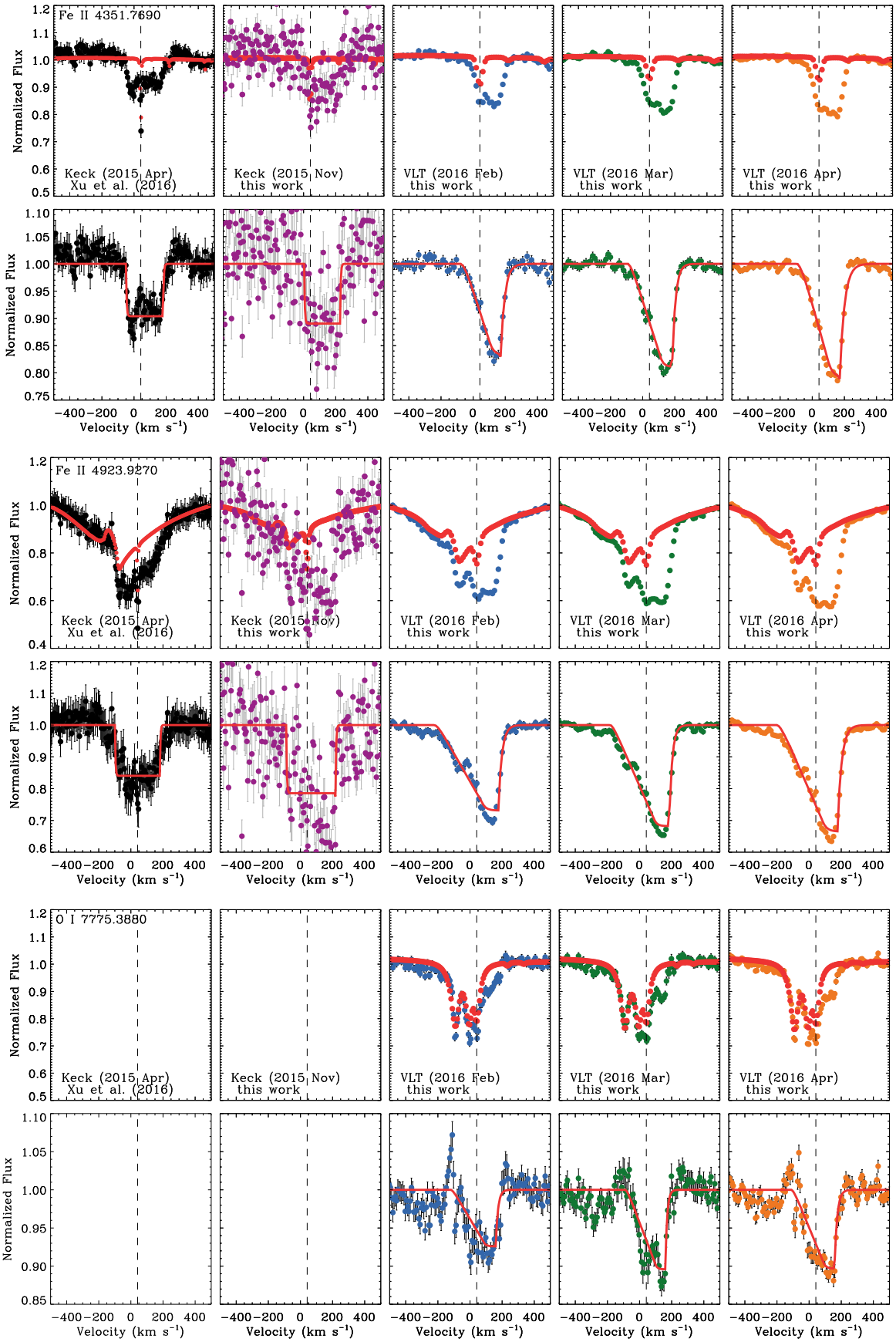

Figure 2. Examples of circumstellar profile fitting. Three lines are shown: Fe II 4351.7 Å (top), Fe II 4923.9 Å (middle), and O I 7775.4 Å (bottom). The top row for each shows the observed spectrum for each epoch with the stellar model overlaid in red. The bottom row of each shows the stellar lines removed, leaving only the circumstellar absorption. A simple trapezoidal model is shown in red (a simple box for the Keck epochs and a trapezoid with a tapered blue edge for the VLT epochs and convolved with the instrumental line spread function).

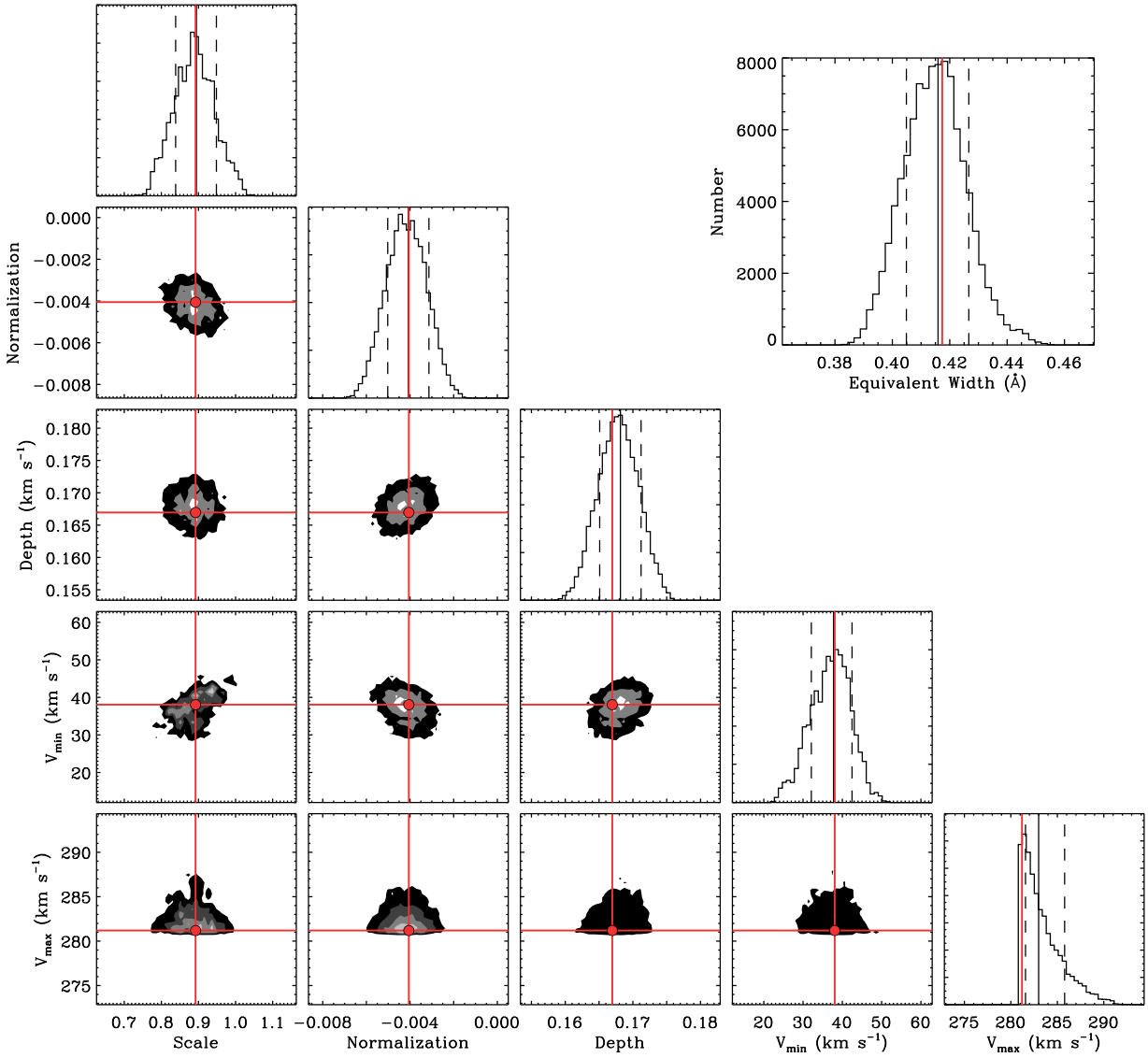

Figure 3. Posterior probability distributions for the five parameters used in the MCMC analysis of a circumstellar line shown in Figure 2. This example is taken from the 2016 February epoch for the Fe II 4351.7 Å line. The red lines indicate the values of the parameters that resulted in the minimum χ^2 value, i.e., the best fit. The solid black line indicates the median value and the dashed lines the 68% confidence intervals. The equivalent width posterior probability distribution is also shown in the upper right. All distributions are well characterized. Note the distinctive asymmetry of the V_{max} distribution, indicative of the extremely sharp velocity cutoff on the red side of the circumstellar absorption profile evidenced in the observed spectra.

the trace hydrogen in the photosphere was delivered in bulk by a parent body with this water fraction, then the total (accreted) planetesimal mass would be 2.4×10^{23} g or about one-quarter the mass of Ceres. This value is in excellent agreement with the total accreted mass as inferred from metals alone, which is 2.6×10^{23} g based on this work, and broadly agrees with previous estimates (Xu et al. 2016).

3.2. Circumstellar

Broad and distinctive circumstellar absorption is clearly present, which bracket and blend with the photospheric lines. The circumstellar absorption is shifted by the systemic velocity of the system ($\approx$12 km s^{-1}) but no significant gravitational redshift (relatively to the observer) is expected at its location. We detect significant (i.e., $>3\sigma$ absorption measured in three or more epochs) circumstellar absorption in more than 250 lines from among 10 elements and 14 ions (O I, Na I, Mg I, Al I, Ca I, Ca II, Ti I, Ti II, Cr II, Mn II, Fe I, Fe II, Ni I, and Ni II). Like optical spectra of the solar atmosphere, the ion that produces the most numerous features is Fe II, with more than 100 transitions with detected circumstellar absorption. The vast majority of detected transitions arise from low excitation energies (<4 eV). Several ground-state transitions are also detected and may be contaminated by absorption from the interstellar medium (Frisch et al. 2011; Johnson et al. 2015). We see circumstellar absorption for O I at 7775.4 Å, though no clear circumstellar absorption is detected for the hydrogen Balmer lines. It is noteworthy that there is circumstellar absorption seen in O I, but not in Hα. While the models used here are not able to link these species to the total atomic abundance in gas, O I is present at $>6 \times 10^{-19}$ g cm^{-3}, whereas for $n = 2$ H I there is an upper limit of 10^{-20} g cm^{-3}.

Table 1 lists candidate identifications for all detected circumstellar features along with the basic details of the electronic transition. We perform a Markov Chain Monte Carlo (MCMC) analysis on all detections. After removal of the stellar

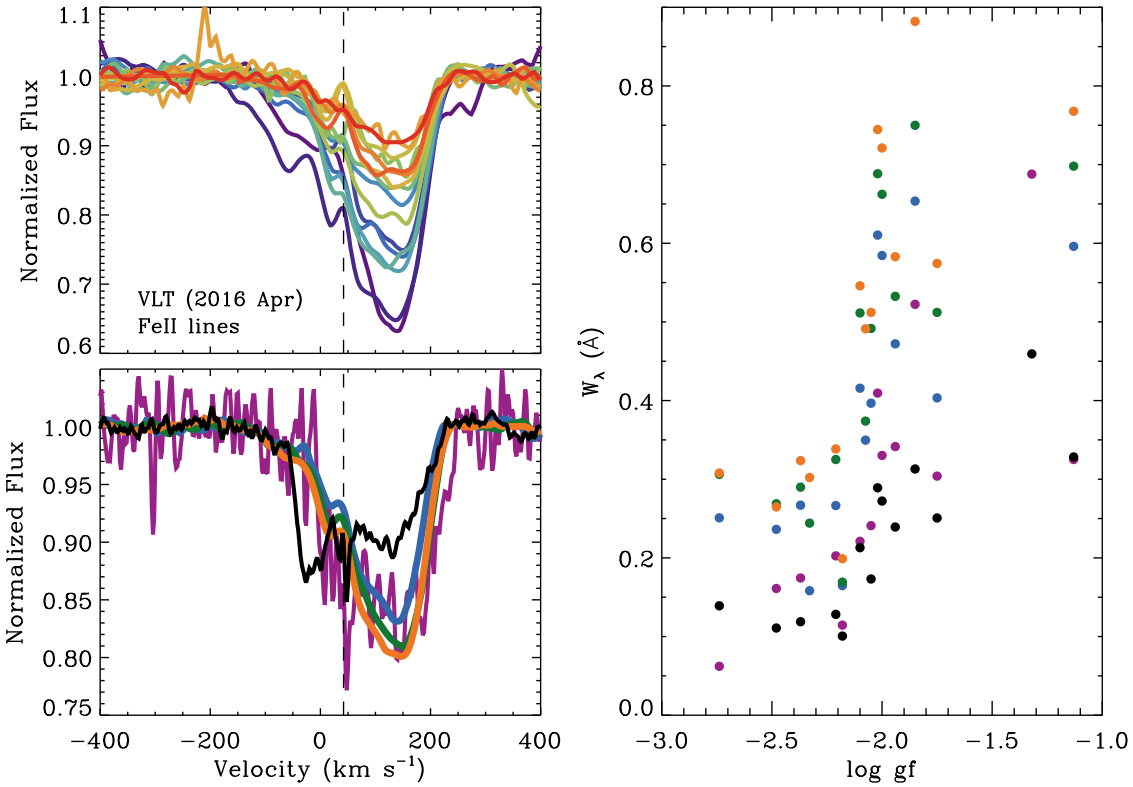

Figure 4. (Top left) Comparison of 16 Fe II circumstellar absorption features observed during the 2016 April epoch, where the color scale is proportional to the oscillator strength. (Bottom left) Mean profiles created by combining all the individual lines shown at top for all five epochs, where the color is the same as in Figure 1. As seen in the individual profiles in Figure 1, significant changes are seen in the circumstellar absorption profiles. (Right) Equivalent width vs. oscillator strength for Fe II. The colors correspond to each epoch, as in the plot on the bottom left. The correlation indicates that the gas is not highly optically thick, though saturation is present at the largest oscillator strengths.

lines, all circumstellar features were fit with a simple trapezoidal model (a simple box for the Keck epochs and a trapezoid with a tapered blue edge for the VLT epochs) in order to characterize the basic traits of the absorption. Three parameters are used to create the trapezoidal model, a minimum velocity, a maximum velocity, and absorption depth. Two additional parameters were fit to optimize the scaling of the stellar photospheric absorption removal and the normalization of the continuum. The profiles are convolved with the appropriate instrumental line spread function. Occasionally, i.e., <5% of fits, the automated normalization procedure does not satisfactorily model the continuum, particularly for dense spectral regions or poor S/N, and while a line is significantly detected, a poor fit results. Low significance and poor fits are indicated by 3σ upper limits and are often caused by blending, and noted as such in Table 1.

A few examples of the fits to the circumstellar absorption are shown in Figure 2. The posterior probability distributions from the MCMC analysis are given in Figure 3 for the 2016 February epoch of the Fe II 4351.7 Å feature. The median and 68% confidence intervals are displayed for each distribution, in addition to the fit that resulted in the minimum χ^2, i.e., the best fit. The posterior probability distributions are well characterized. Note the strong asymmetry in the maximum velocity parameter, signifying the sharp edge on the redward side of the observed circumstellar absorption profile. The MCMC analysis shows that there are no strong correlations among the fitted absorption parameters and provides a quantitative description of the parameters and their errors. The equivalent width is calculated from this fit and given in Table 1. The full table has fits to all lines and gives the median values and 68% confidence intervals for all parameters (e.g., minimum and maximum velocity and depth of absorption). Due to the high density of circumstellar lines, blends are common, and complicate the fit values. Blends are noted in the table, while isolated features give robust fits.

4. Circumstellar Absorption Variability

Observations over five epochs make it clear that the circumstellar absorption is varying over month-long timescales.

4.1. Monthly Variability

In order to evaluate the detailed line profile and variation between epochs, Figure 4 displays a sequence of Fe II lines that are strong, unblended, and relatively isolated from other features. The sequence of transitions are shown overlaid in the top left for the 2016 April epoch. For all epochs a mean profile is produced and overlaid in the bottom left panel. The basic properties are

1. a broad absorption feature that is roughly 225 km s^{-1} in width;
2. a range of line depths up to 35% of the continuum;
3. a constant and sharp maximum velocity of ≈210 km s^{-1} (with a standard deviation of 85 km s^{-1}) in the early epochs and ≈270 km s^{-1} (with a standard deviation of 23 km s^{-1}) in the late epochs, relative to the heliocentric rest frame; and

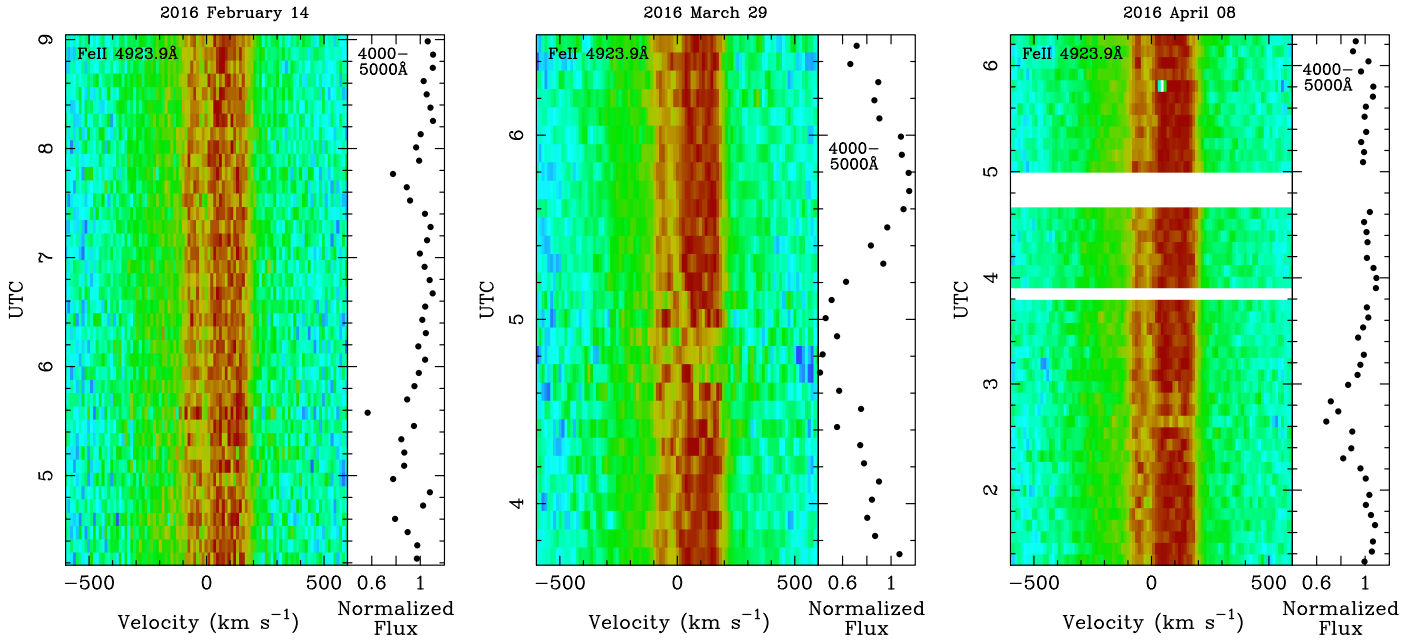

Figure 5. Running comparison of the Fe II 4923.9 Å spectral region for each epoch. Left: 2016 February 14, middle: 2016 March 29, and right: 2016 April 8. Green colors indicate unity in the normalized spectrum, whereas the darkest red colors indicate absorption approximately 40% below the normalized continuum. Momentary (i.e., tens of minutes) departures from the mean profile are detected in both the 2016 March and April observations. Broadband (4000–5000 Å) spectrophotometry is included in the narrow right panel for each epoch. The circumstellar line variability is clearly associated with the photometric transit events that have been seen on ≈4.5 hr periods.

4. a minimum velocity of $\approx -5\,\mathrm{km\,s^{-1}}$ in the early epochs and $\approx 40\,\mathrm{km\,s^{-1}}$ in the late epochs, relative to the heliocentric rest frame.

The long-term (i.e., monthly) evolution of the absorption tends toward deeper absorption on the red side of the circumstellar feature over time, while the maximum velocity increases slightly. The strong blueshifted circumstellar absorption (between -50 and $0\,\mathrm{km\,s^{-1}}$) observed in the early epochs has disappeared, and while the minimum velocity remains similar, the tapered appearance of the most recent data make this difficult to accurately measure. This distinct change in the blue side of the circumstellar absorption line shape occurs between 2015 November and 2016 February. In our simple trapezoidal fitting of the line profile, the two 2015 epochs are fit with a simple rectangular shape, whereas the 2016 epochs are fit with a trapezoid with a tapered slope on the blue side.

Aside from the changes in the spectral line shape, the total absorption (i.e., equivalent width) is systematically increasing with time. The last three epochs increase 15%–20% from month to month. As the transiting source material clearly continues to evolve, there is likely a continuous deposition of material that is feeding and growing the disk of gas that is responsible for this circumstellar absorption. As shown in Figure 4, there is a correlation in the equivalent width with oscillator strength. Therefore, the absorption is not extremely optically thick, with a median optical depth $\tau \approx 2$.

4.2. Momentary Variability

Our most recent observations also provide clear evidence of circumstellar variation on short timescales (i.e., tens of minutes). Our most recent epochs include coverage of between three and five hours (slightly more than the orbital period of the transiting objects), and momentary changes in the line profile are detected most dramatically in the 2016 March observations. Figure 5 shows time-resolved spectra of the Fe II 4923.9 Å line for all three of the most recent epochs. Short-term variability is clearly detected in 2016 March over a period of approximately 20 minutes, roughly 10% of the entire observation. Exposures at 4.7 and 4.8 UTC are the only profiles that show $>3\sigma$ variations from the mean profile in a significant fraction (i.e., >10%) of velocities across the circumstellar profile. At no other times are more than 10% of the velocities discrepant from the mean profile by more than 3σ. Although the maximum velocity remains the same, the variability is characterized by a significant decrease in absorption on the red side of the profile, between 60 and $170\,\mathrm{km\,s^{-1}}$. No significant variation is measured in the 2016 February observations (i.e., no exposure show more than 10% of the velocities across the profile show departures from the mean profile $>3\sigma$). The 2016 April observations shows significant variability at 2.7 UTC, where 23% of the velocities across the profile show departures $>3\sigma$ from the mean profile, again on the redward side of the profile between 100 and $170\,\mathrm{km\,s^{-1}}$.

These momentary variations coincide with marked decreases in the spectrophotometric flux summed across all wavelengths, and corresponds in time to the most significant photometric transit signatures (Gänsicke et al. 2016; Rappaport et al. 2016). The decrease in line absorption can be explained if an opaque body, like the parent body and other planetesimals that are causing the photometric transit signatures, blocks a fraction of the gas disk causing the absorption. This implies that the absorbing gas is closer to the white dwarf than the obscuring, transiting objects. Our exposure times are significantly longer than those for the photometric monitoring, but the variation does persist over a few exposures (i.e., tens of minutes). It is worth noting the rarity of such events, and that for much of the observed period, the circumstellar absorption profile remained remarkably constant.

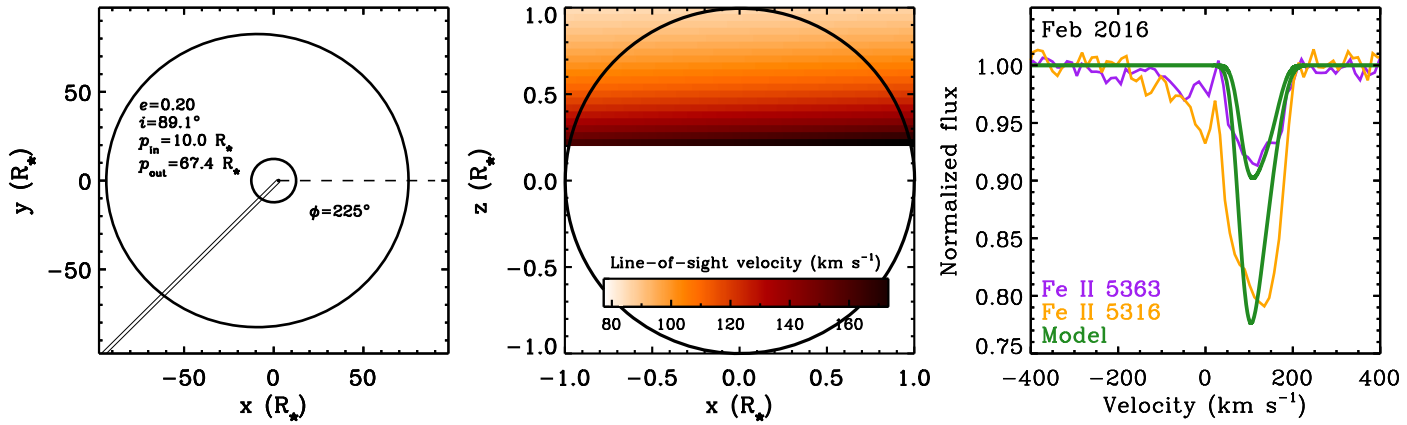

Figure 6. Model of a low eccentricity disk surrounding WD 1145+017 that successfully reproduces the observed profile shape and line ratios. (Left) Geometry of the disk, extending from 10.0 $R_\star$ to 67.4 $R_\star$. (Middle) Projected stellar disk with shading to indicate the radial velocity of disk. Note the disk is slightly inclined. The observed asymmetric velocity profile can be produced with a line of sight near the apsis of the orbit. (Right) Comparison of the model to two Fe II lines showing that the profile shape and line ratios are well characterized.

5. A Model of the Circumstellar Environment of WD 1145+017

We explore three model possibilities to explain the spectral signature of the circumstellar material: (1) discrete streams, either magnetically or gravitationally formed (e.g., Blinova et al. 2016); (2) a curtain of magnetospheric accretion (Warner 2004; Bouvier et al. 2007) with a disk wind (Kwan et al. 2007); (3) an eccentric or warped disk (Metzger et al. 2012; Gänsicke et al. 2008).

The accretion streams seem unlikely given that we do not see much short-term variability. Even for modestly magnetic stars, these are likely narrow features that would rotate with the star. The rotation period of the star (typically a few days; Greiss et al. 2014) is likely too long to be smeared over a single exposure. So, due to the near-constancy of the absorption over five hours, with only short departures from the mean absorption profile, this configuration is unlikely. In addition, we do not expect that this system is unstable to magnetic Rayleigh–Taylor instabilities (Blinova et al. 2016), given that the corotation radius is well beyond reasonable estimates of the magnetospheric radius.

Magnetospheric accretion models are routinely used to describe mass accretion onto pre-main-sequence stars (e.g., Hartmann et al. 1994; Muzerolle et al. 2004; Fischer et al. 2008) and have also been explored for white dwarfs (Patterson 1994; Warner 2004). This model is attractive since the nearly edge-on orientation of the WD 1145+017 system results in an abrupt redshifted velocity cutoff where the accreting material flows above and below the limits of the stellar disk, a feature that is seen in all of the circumstellar lines. Disk winds launched from the interaction region of the stellar magnetic field and the gas disk are also a common feature of magnetospheric accretion (e.g., Kwan et al. 2007; Kurosawa et al. 2016) and could be producing the narrow blueshifted absorption seen in some of the spectra. We have explored model absorption line profiles produced by an aligned dipolar magnetospheric accretion flow and find that the observed line profiles are inconsistent with this geometry. The inconsistency is mainly due to the difficulty of reproducing the sharp red velocity edge. While we expect magnetospheric accretion to occur in this system and is a likely mechanism for accretion onto the star, it cannot solely account for the observed profiles.

Finally, we have constructed an eccentric disk model to explain the observed line profiles. The disk is composed of slightly inclined confocal ellipses that extend from an inner to an outer radius. We assume that the density is azimuthally uniform and decreases linearly with radius. The absorption profiles are approximated as Doppler-broadened delta functions with an intrinsic line broadening of 15 km s^{-1}. The vertical thickness of the disk is 0.1 R_*. The stellar parameters are taken from Vanderburg et al. (2015).

The model profiles for two Fe II lines observed in 2016 February, with different oscillator strengths are shown in Figure 6 (right panel, thick green lines). We find that a slightly inclined, mildly eccentric disk viewed at 41° from the apsidal line is able to roughly reproduce the velocity range and depth of the observed redshifted absorption. Note that there is a degeneracy between the viewing angle and the eccentricity, and we have chosen to demonstrate this model with a relatively low eccentricity disk. We do not attempt to model the blueshifted absorption. We note that the size of our favored disk (see Figure 6) has similar dimensions to that derived by Melis et al. (2010) for SDSS J104341.53+085558.2. The truncation radius of $\approx 10 R_\star$ may be dictated by the magnetosphere (Bouvier et al. 2007), with reasonable values for magnetic field (e.g., 130 G) and accretion rate (e.g., 10^{10} g s^{-1}). Note that current observations are only sensitive to magnetic field strengths $\gtrsim$ a few kG (Landstreet et al. 2016), and therefore this field would go undetected. The total Fe II mass in the model disk is 1.1×10^{14} g (a minimum value given that even a modest disk inclination will result in only part of the disk projected on the stellar disk), suggesting a total disk mass less than the mass of Ceres ($M_{\rm Ceres} \approx 10^{24}$ g). This value is in agreement with the mass as inferred from the photospheric lines in Section 3.1.

5.1. Explaining the Variability

A simple eccentric disk model is capable of explaining both the long- and short-term variability that is observed in the circumstellar absorption. The monthly variability has two components. The changes in the absorption depth can be explained by density changes of a factor of 3–8× the nominal level. Because we know that larger transiting bodies are evolving and presumably disintegrating, these density variations could be a result of the gradual feeding of material to the disk by the bodies being disrupted. Alternatively, or in

addition, general relativity may alter the orbital dynamics, particularly in the inner disk on timescales of months (Veras 2016). Precession or other effects may also contribution to the modest changes we see between epochs. The other long-term variability that is seen is the absorption profile to the blue of the photospheric line. This feature is not accounted for in our eccentric disk model, but as discussed above, could be due to a disk wind associated with magnetospheric accretion. Changes in disk properties and accretion rates could account for changes in the disk wind absorption strength. The momentary variability that is seen in the 2016 March and 2016 April observations are coincident with a decrease in flux at all wavelengths, similar to the transit signatures detected in the photometric campaigns. The spectral variability, notably the reduced absorption at the highest velocities, can be explained by a momentary shielding of the disk by an opaque, transiting body beyond the gas disk.

6. Conclusions

We present five epochs of high resolution and high signal-to-noise spectroscopy of the white dwarf WD 1145+017, discovered to exhibit transiting signals of orbiting material. The most significant conclusions are as follows.

1. We detect variation in the WD 1145+017 circumstellar gas disk absorption over timescales ranging from minutes to months. A systematic increase in equivalent width is measured over the course of the year from 2015 April to 2016 April. In addition, significant changes in the profile shape are seen, notably a significant increase in the absorption depth on the red side of the feature and the disappearance of absorption on the blue side of the line seen in the earliest epochs.
2. Circumstellar absorption is measured in more than 250 transitions for 14 different ions of 10 different elements. We fit the circumstellar absorption with a simple trapezoidal profile and detect significant long-term variability across a period of a year. Detected absorption arises from transitions with low excitation energies, the vast majority from <4 eV. A correlation between equivalent width and oscillator strength is found and indicates that the absorption is not strongly optically thick (median $\tau \approx 2$).
3. Short-term variability, on the timescale of minutes, is detected in two of the three most recent epochs. WD 1145+017 is monitored for over 5 hr each time and momentary departures from the stable absorption feature are detected.
4. We present a model of the circumstellar gas disk that involves an eccentric disk and magnetospheric accretion to explain the broad profile and modest absorption depth.

This work is an initial look at a rich data set on a unique target, because at this time, WD 1145+017 remains the only known white dwarf with detected transit signatures. Future work will involve a comprehensive chemical inventory of both the accreted and circumstellar material. The detection of O I is noteworthy. High S/N observations could potentially lead to detections or stringent upper limits on hydrogen, putting interesting constraints on the volatile content. In addition, the spectroscopic monitoring of the accretion should be correlated and compared to the detected photometric variability. WD 1145+017 offers the unprecedented opportunity to investigate in detail the disruption of an exoplanetesimal in real time, to constrain models of the physical and temporal processes; the production of dust and gas, and the eventual accretion onto the star.

We wish to thank the referee for their thoughtful review. Some of the data presented herein were obtained at the W.M. Keck Observatory from telescope time allocated to the National Aeronautics and Space Administration through the agency's scientific partnership with the California Institute of Technology and the University of California. This work was supported by a NASA Keck PI Data Award, administered by the NASA Exoplanet Science Institute. The Observatory was made possible by the generous financial support of the W.M. Keck Foundation. The authors wish to recognize and acknowledge the very significant cultural role and reverence that the summit of Mauna Kea has always had within the indigenous Hawaiian community. We are most fortunate to have the opportunity to conduct observations from this mountain. Some of the data presented herein were made with ESO Telescopes at the La Silla Paranal Observatory under programme ID 296.C-5014. The authors wish to thank Detlev Koester for generating the white dwarf spectral models used in this work and for his other helpful contributions to the project. S.G.P. acknowledges financial support from the European Research Council under the European Union's Seventh Framework Programme (FP/2007–2013) under ERC-2013-ADG Grant Agreement no. 340040. The research leading to these results has received funding from the European Research Council under the European Union's Seventh Framework Programme (FP/2007–2013)/ERC Grant Agreement n. 320964 (WDTracer). This work was completed with support from the National Science Foundation through Astronomy and Astrophysics Research Grant AST-1313268 (PI: S.R.).

Facilities: Keck:I (HIRES), VLT: (X-shooter).

Software: IRAF, IDL.

References

Alonso, R., Rappaport, S., Deeg, H. J., & Palle, E. 2016, A&A, 589, L6
Bergfors, C., Farihi, J., Dufour, P., & Rocchetto, M. 2014, MNRAS, 444, 2147
Blinova, A. A., Romanova, M. M., & Lovelace, R. V. E. 2016, MNRAS, 459, 2354
Bouvier, J., Alencar, S. H. P., Harries, T. J., Johns-Krull, C. M., & Romanova, M. M. 2007, in Protostars and Planets V, ed. B. Reipurth, D. Jewitt, & K. Keil (Tucson, AZ: Univ. Arizona Press), 479
Carson, J., Thalmann, C., Janson, M., et al. 2013, ApJL, 763, L32
Croll, B., Dalba, P. A., Vanderburg, A., et al. 2017, ApJ, 836, 82
Debes, J. H., & López-Morales, M. 2008, ApJL, 677, L43
Farihi, J., Gänsicke, B. T., & Koester, D. 2013a, Sci, 342, 218
Farihi, J., Gänsicke, B. T., & Koester, D. 2013b, MNRAS, 432, 1955
Farihi, J., Gänsicke, B. T., Wyatt, M. C., et al. 2012, MNRAS, 424, 464
Farihi, J., Jura, M., & Zuckerman, B. 2009, ApJ, 694, 805
Fischer, W., Kwan, J., Edwards, S., & Hillenbrand, L. 2008, ApJ, 687, 1117
Frisch, P. C., Redfield, S., & Slavin, J. D. 2011, ARA&A, 49, 237
Gänsicke, B. T., Aungwerojwit, A., Marsh, T. R., et al. 2016, ApJL, 818, L7
Gänsicke, B. T., Koester, D., Farihi, J., et al. 2012, MNRAS, 424, 333
Gänsicke, B. T., Koester, D., Marsh, T. R., Rebassa-Mansergas, A., & Southworth, J. 2008, MNRAS, 391, L103
Gänsicke, B. T., Marsh, T. R., Southworth, J., & Rebassa-Mansergas, A. 2006, Sci, 314, 1908
Greiss, S., Gänsicke, B. T., Hermes, J. J., et al. 2014, MNRAS, 438, 3086
Hartmann, L., Hewett, R., & Calvet, N. 1994, ApJ, 426, 669
Johnson, M. C., Redfield, S., & Jensen, A. G. 2015, ApJ, 807, 162
Jura, M., & Young, E. D. 2014, AREPS, 42, 45
Kipping, D. M., Torres, G., Buchhave, L. A., et al. 2014, ApJ, 795, 25
Klein, B., Jura, M., Koester, D., Zuckerman, B., & Melis, C. 2010, ApJ, 709, 950

Koester, D. 2009, A&A, 498, 517
Koester, D. 2010, MmSAI, 81, 921
Koester, D., Gänsicke, B. T., & Farihi, J. 2014, A&A, 566, A34
Kurosawa, R., Kreplin, A., Weigelt, G., et al. 2016, MNRAS, 457, 2236
Kwan, J., Edwards, S., & Fischer, W. 2007, ApJ, 657, 897
Landstreet, J. D., Bagnulo, S., Martin, A., & Valyavin, G. 2016, A&A, 591, A80
Macintosh, B., Graham, J. R., Barman, T., et al. 2015, Sci, 350, 64
Madhusudhan, N., Lee, K. K. M., & Mousis, O. 2012, ApJL, 759, L40
Madhusudhan, N., & Redfield, S. 2015, IJAsB, 14, 177
Manser, C. J., Gänsicke, B. T., Marsh, T. R., et al. 2016, MNRAS, 455, 4467
Marois, C., Macintosh, B., Barman, T., et al. 2008, Sci, 322, 1348
Melis, C., Jura, M., Albert, L., Klein, B., & Zuckerman, B. 2010, ApJ, 722, 1078
Metzger, B. D., Rafikov, R. R., & Bochkarev, K. V. 2012, MNRAS, 423, 505
Miller-Ricci, E., & Fortney, J. J. 2010, ApJL, 716, L74
Muzerolle, J., D'Alessio, P., Calvet, N., & Hartmann, L. 2004, ApJ, 617, 406
Öberg, K. I., Guzmán, V. V., Furuya, K., et al. 2015, Natur, 520, 198
Patterson, J. 1994, PASP, 106, 209
Raddi, R., Gänsicke, B. T., Koester, D., et al. 2015, MNRAS, 450, 2083
Rappaport, S., Gary, B. L., Kaye, T., et al. 2016, MNRAS, 458, 3904
Redfield, S., Endl, M., Cochran, W. D., & Koesterke, L. 2008, ApJL, 673, L87
Rocchetto, M., Farihi, J., Gänsicke, B. T., & Bergfors, C. 2015, MNRAS, 449, 574
Su, K. Y. L., Rieke, G. H., Malhotra, R., et al. 2013, ApJ, 763, 118
van der Marel, N., van Dishoeck, E. F., Bruderer, S., et al. 2013, Sci, 340, 1199
Vanderburg, A., Johnson, J. A., Rappaport, S., et al. 2015, Natur, 526, 546
Vanderburg, A., Latham, D. W., Buchhave, L. A., et al. 2016, ApJS, 222, 14
Veras, D. 2016, RSOS, 3, 150571
Veras, D., Leinhardt, Z. M., Eggl, S., & Gänsicke, B. T. 2015, MNRAS, 451, 3453
Vernet, J., Dekker, H., D'Odorico, S., et al. 2011, A&A, 536, A105
Vogt, S. S., Allen, S. L., Bigelow, B. C., et al. 1994, Proc. SPIE, 2198, 362
von Hippel, T., & Thompson, S. E. 2007, ApJ, 661, 477
Warner, B. 2004, PASP, 116, 115
Wilson, D. J., Gänsicke, B. T., Koester, D., et al. 2014, MNRAS, 445, 1878
Wyatt, M. C., Farihi, J., Pringle, J. E., & Bonsor, A. 2014, MNRAS, 439, 3371
Xu, S., & Jura, M. 2012, ApJ, 745, 88
Xu, S., & Jura, M. 2014, ApJL, 792, L39
Xu, S., Jura, M., Dufour, P., & Zuckerman, B. 2016, ApJL, 816, L22
Xu, S., Jura, M., Klein, B., Koester, D., & Zuckerman, B. 2013, ApJ, 766, 132
Zuckerman, B., Melis, C., Klein, B., Koester, D., & Jura, M. 2010, ApJ, 722, 725